Department of Precision and Microsystems Engineering

Frequency Domain Analysis and Design of Fixed Phase Reset Control

Hsing-Li Hsu

Report no : 2023.097
Coach : Xinxin Zhang
Professor : Dr. Hassan HosseinNia
Specialisation : Engineering Dynamics
Type of report : MSc Thesis
Date : 10 November 2023

CONTENTS

PREFACE

This report signifies the completion of my studies in the High-Tech Engineering track at TU Delft, marking the final stage of my master's program. As I reflect on my time at TU Delft, I am grateful for the experiences and knowledge I have gained. Each moment, whether in my personal life or academic pursuits, has had a profound impact on me.

Throughout this journey, I have received support and guidance from individuals who have played pivotal roles in shaping my growth. I would like to express my heartfelt gratitude to the following people:

Xinxin Zhang: I want to express my heartfelt appreciation to my daily supervisor, Xinxin Zhang. Your professional guidance and patient support during our meetings have been immensely valuable to me. Whenever I faced difficulties or felt discouraged, your encouragement motivated me to keep moving forward. I am truly grateful for your assistance and commitment to my progress. Thank you for being an exceptional mentor and for playing a significant role in my journey.

Hassan HosseinNia: I am grateful for the opportunity you have given me to work on such an exciting project where I could apply the knowledge I gained at TU Delft. Your constant encouragement to express my thoughts and ideas has greatly benefited me. I want to express my thanks for your support and for providing me with this invaluable learning experience.

Friends and Family: I am deeply appreciative of the support and encouragement from my friends and family throughout this period. Their unwavering belief in me has been a constant source of motivation, helping me overcome challenges and remain focused on my studies.

I extend my sincere appreciation to everyone who has been a part of my journey at TU Delft. Their valuable contributions, support, and guidance have played a vital role in my personal and academic development. I am profoundly grateful for their assistance, and I will carry the knowledge and experiences gained during my time at TU Delft as I embark on future endeavors in the field of high-tech engineering.

Hsing-Li Hsu
November 10, 2023

1

INTRODUCTION

Abstract—Reset controllers are acknowledged for their potential to enhance performance, like speed and precision in precision motion industries. Existing literature primarily utilizes the classical zero-crossing law in these controllers. This study introduces a novel reset component, termed "fixed-phase reset control", which employs an innovative reset mechanism distributing multiple resets within a single period under sinusoidal inputs. To analyze the performance of the new controller, we've developed a new higher-order sinusoidal describing function analysis method. Through simulations, the accuracy of this analytical approach is verified. Additionally, the results demonstrated the significant improvements of the new reset controller in convergence and tracking capabilities compared to traditional reset controllers.

Accuracy and speed are critical requirements within the semiconductor industry. An exemplary application is the employment of a magnetically levitated wafer table in the EUV lithography machine [1], ensuring precise and swift wafer transportation. Specifically, sensors measure a wafer's position at a rapid rate of 20,000 times per second with an accuracy of around 60 picometers. Achieving such high precision and speed demands significant research in precision position technology. Controllers play a pivotal role in fulfilling these requirements.

1

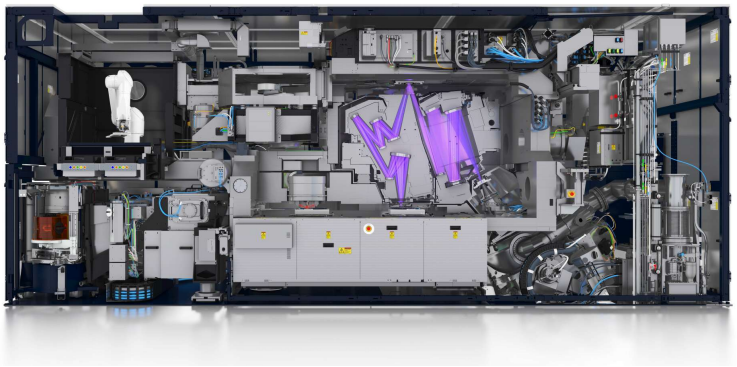

Figure 1.1: TWINSCAN NXE:3400B [1]

Linear controllers, such as PID controllers, are widely used in industrial settings due to their simplicity and ease of tuning. However, traditional linear control systems exhibit limitations associated with Bode's phase-gain relationship [2]. As an alternative, reset control shows promise to break out the linear limitations. The initial reset control, Clegg Integrator, introduced by J.C. Clegg in the 1950s [3], possesses a distinct characteristic compared to conventional integrators. Notably, its first-order harmonic exhibits a phase lag of -38° while maintaining a -20 dB/decade slope, challenging Bode's phase-gain relationship and offering potential enhancements to control system performance.

To broaden the applicability of the Clegg integrator, Horowitz introduced the first-order reset element (FORE) [4], [5]. This component, known as the FORE, has exhibited promising results in mitigating high-frequency noise. Furthermore, ongoing research in the field of reset control has given rise to various reset controller variants, see [6], [7], [8], [9].

There are some tries including [10], [12], [13], and [14], which have explored the effect of modifying the timing of reset actions. The results show the effectiveness of predetermined reset instant [10, 12] has superior performance in PZT positioning stages. However, there is a lack of a clear definition of the new resetting mechanism as well as frequency-domain analysis tools for this variant. Additionally, due to the predetermined reset instant, specific input frequencies will not benefit from the advantageous effects of the reset action.

To address this limitation, we propose a novel type of reset control law named Fixed Phase Reset Control (FPRC). The contribution of this paper includes:

1. The development of higher-order sinusoidal input describing function (HOSIDF) for FPRC.
2. Validating the calculation method of HOSIDF by simulation results.
3. conducting numerical simulations to validate the effectiveness of FPRC.

These studies introduce innovative methodologies to optimize the functionality and effectiveness of reset control systems across diverse applications. While numerous studies have addressed stability issues in reset systems, as evidenced by [15], [16], [17], [18],

it's important to note that the primary focus of this paper is not on stability analysis, and therefore, we will not extensively delve into this topic.

The structure of this study is outlined as follows. Section chapter 2 introduces the background knowledge of reset control systems, including state space representation and frequency domain analysis tools. Section chapter 3 outlines the principal contributions of this research, which encompass (1) the definition of the fixed phase reset control law, and (2) the derivation of the frequency domain model for FPRC systems. Section chapter 4 shows the accuracy of the developed HOSIDF. Section chapter 5 presents numerical simulation results to confirm the effectiveness of FPRC. Finally, Section chapter 6 presents the conclusions drawn from this study and outlines directions for future work.

2

BACKGROUND

2.1. LIMITATION OF LINEAR CONTROLLER

Linear control systems are extensively utilized; however, they are not without limitations. One of the prominent constraints is associated with Bode's phase-gain relationship [2]. The Bode plot of a system is conventionally segmented into three regions for assessment. As mentioned earlier, to effectively trace a low-frequency reference signal, the system's magnitude needs to be high at low frequencies. Simultaneously, to suppress high-frequency noise, the system's magnitude should be low at higher frequencies.

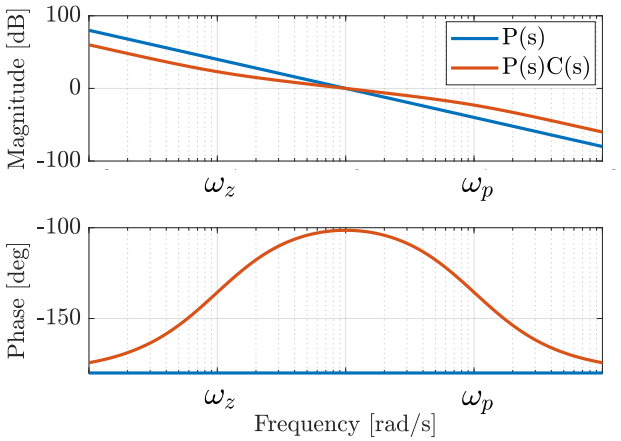

Figure 2.1: Trade-off between robustness and performance.

Fig. 2.1 illustrates that, without the addition of any controller ($P(s)$), the system's phase is consistently -180 degrees across all frequencies, which is suboptimal for stability. Introducing a lead-lag controller ($C(s)$) resolves this phase issue, but concurrently, it

adversely affects the system's magnitude. At lower frequencies, the tracking performance deteriorates as the system's magnitude experiences a slight decrease. Additionally, high-frequency noise gets amplified.

It has been demonstrated that robustness and performance are inversely related, suggesting that there exists a trade-off between these two attributes. This implies that, in order to optimize a system's performance, one must necessarily accept a certain level of reduced robustness, and vice versa.

2.2. DEFINITION OF RESET CONTROL SYSTEMS

The block diagram of a closed-loop reset control system (RCS) is depicted in Fig. 2.2. This system comprises several components: a plant denoted as P, a controller labeled as C, a reference signal represented by $r(t)$, an error signal indicated as $e(t)$, a control input signal designated as $u(t)$, a disturbance signal denoted as $d(t)$, measurement noise characterized as $n(t)$, and a measured output tracked as $y(t)$.

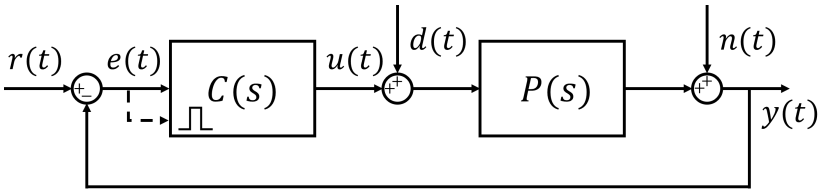

Figure 2.2: Block diagram of a closed-loop reset control system, where the dashed arrow represents the reset action.

The state-space representation of a reset controller in Fig. 2.2 can be written as follows:

$$C = \begin{cases} \dot{x}_r(t) = A_R x_r(t) + B_R e(t), & e(t) \neq 0 \\ x_r(t^+) = A_\rho x_r(t), & e(t) = 0 \\ u(t) = C_R x_r(t) + D_R e(t) \end{cases} \tag{2.1}$$

$x_r(t) \in \mathbb{R}^{n_C}$ is the state of the reset controller and A_R, B_R, C_R, D_R are the state matrices. A_ρ is defined as the reset matrix:

$$A_\rho = \begin{bmatrix} I_{nr} & \\ & \gamma_r \end{bmatrix}, \gamma = \text{diag}(\gamma_1, \gamma_1, ..., \gamma_r) \tag{2.2}$$

γ_r and I_{nr} represent reset states and non-reset states, respectively. Here, r denotes the number of reset states, nr represents the number of non-reset states, and the total number of states is given by $n_C = r + nr$. It's important to note that in this study, we restrict our discussion to the case where $\gamma = 0$.

The state space representation of the plant in Fig. 2.2 can be expressed as follows:

$$P = \begin{cases} \dot{x}_p(t) = A_P x_p(t) + B_P u(t) \\ y_p(t) = C_P x_p(t) \end{cases} \tag{2.3}$$

$x_P \in \mathbb{R}^{n_P}$ is the state of the plant. By combining the controller (1) and the plant (2), the state space representation of a closed-loop reset control system can be expressed as follows:

$$H = \begin{cases} \dot{x}(t) = A_{cl}x(t), & x \notin J \\ x(t^+) = A_{\rho cl}x(t), & x \in J \\ y(t) = C_{cl}x(t) \end{cases} \tag{2.4}$$

where

$$A_{cl} = \begin{bmatrix} A_R & -B_R C_P \\ B_R C_P & A_P \end{bmatrix}, \quad C_{cl} = \begin{bmatrix} 0 & C_P \end{bmatrix} \tag{2.5}$$

$$A_{\rho cl} = \begin{bmatrix} A_\rho & \\ & I \end{bmatrix} \text{ and } J := \{x^T = [x_r^T \; x_p^T] \in \mathbb{R}^{n_C+n_P} | C_{cl}x = 0\} \tag{2.6}$$

2.3. FREQUENCY-DOMAIN ANALYSIS METHOD FOR RCSS

To design a reset control system, the loop shaping method is employed, utilizing describing functions tailored for nonlinear systems. Specifically, the sinusoidal input describing function, which represents the ratio of the phasor output to the phasor input at a given frequency, is applied in this context [28]. This method focuses solely on the first-order harmonic of the Fourier-transformed response. For instance, the describing function of a Clegg integrator is formulated as follows:

$$CI(\omega) = \frac{1}{j\omega}(1 + j\frac{4}{\pi}) = \frac{1.62}{\omega}\angle -38° \tag{8}$$

Guo [19] provided an analytical way to calculate the first-order describing function (DF) for reset systems, as shown in Proposition 1.

Proposition 1. *The DF of an open-loop SISO reset controller $\mathscr{C}$ under a sinusoidal input signal $e(t) = |E|\sin(\omega t + \angle E)$ is given by*

$$\begin{aligned} H(\omega) &= C_R(j\omega I - A_R)^{-1}(I + j\Theta_D(\omega))B_R + D_R \\ \text{with} \quad \Theta_D(\omega) &= -\frac{2\omega^2}{\pi}\Delta(\omega)[\Gamma_r(\omega) - \Lambda^{-1}(\omega)] \\ \Lambda(\omega) &= \omega^2 I + A_R^2 \\ \Delta(\omega) &= I + e^{\frac{\pi}{\omega}A_R} \\ \Delta_r(\omega) &= I + A_\rho e^{\frac{\pi}{\omega}A_R} \\ \Gamma_r(\omega) &= \Delta_r^{-1}(\omega)A_\rho\Delta(\omega)\Lambda^{-1}(\omega) \end{aligned} \tag{2.7}$$

Fig. 2.3 demonstrated this by presenting the output of a Clegg integrator with a $u(t) = \sin(t)$ input, alongside its first-order describing function. It is evident that the output of the first-order describing function and the output of the Clegg Integrator has a huge difference. This is due to the fact that the higher-order terms are neglected, thus the describing function can not accurately represent the sharp edge of the reset action.

For the analysis of higher-order harmonics in open-loop reset control systems, Kars [20] introduced the higher-order sinusoidal describing functions (HOSIDF) analysis method

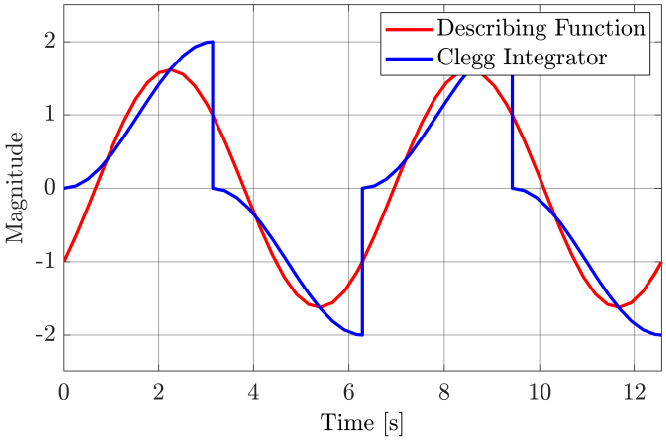

Figure 2.3: Comparison of real output and first-order describing function of a Clegg integrator.

for reset control systems by applying the virtual harmonic generator technique [21], as illustrated in Proposition 2.

Proposition 2. *The HOSIDF of an open-loop SISO reset controller $\mathscr{C}$ under a sinusoidal input signal $e(t) = |E|\sin(\omega t + \angle E)$ is given by*

$$H_n(\omega) = \begin{cases} C_R(j\omega I - A_R)^{-1}(I + j\Theta_D(\omega))B_R + D_R, & For\ \ n = 1 \\ C_R(j\omega n I - A_R)^{-1} j\Theta_D(\omega) B_R, & For\ \ odd\ \ n \geq 2 \\ 0, & For\ \ even\ \ n \geq 2 \end{cases} \tag{2.8}$$

where n is the number of harmonics and ω is the input signal frequency. When $n = 1$, HOSIDF is equal to DF.

With the inclusion of higher-order terms, it becomes straightforward to know the dominant harmonic in various frequency ranges. Fig. 2.5a presents the frequency response of a C.I, while Fig. 2.5b illustrates the frequency response of a Clegg integrator with a second-order plant. Fig. 2.5a indicates no clear dominance of a specific harmonic. In contrast, Figure 2.5b demonstrates that, at low frequencies, higher-order harmonics surpass the first-order harmonic, emphasizing the significance of considering higher-order terms.

Moreover, Xinxin [23] introduced a pulse-based model designed to differentiate between the linear and nonlinear outputs of reset control systems. This model provides a comprehensive insight into the components of a reset control system's output.

Proposition 3. *The transfer function of a SISO reset controller $\mathscr{C}$ in open-loop under a sinusoidal input signal $e(t) = |E|\sin(\omega t + \angle E)$ can be separated into linear and nonlinear*

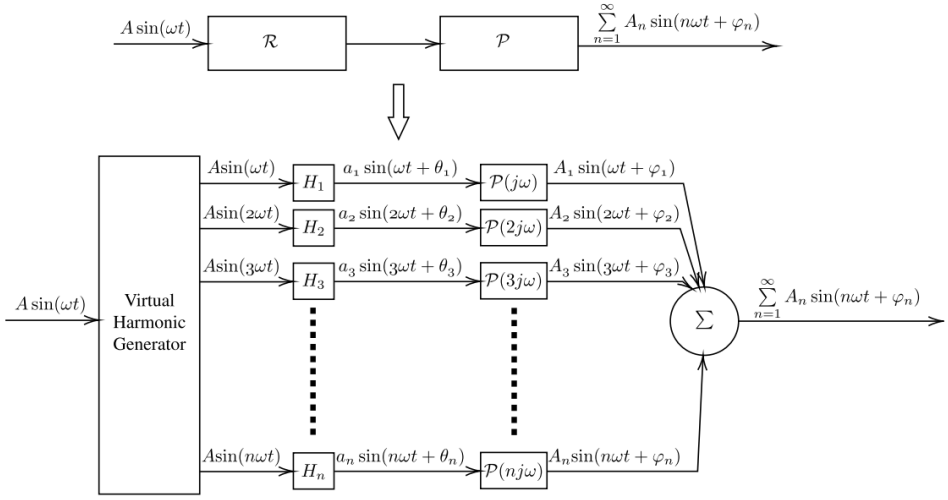

Figure 2.4: Representation of Higher-order sinusoidal-input describing function for open-loop reset control systems. [26]

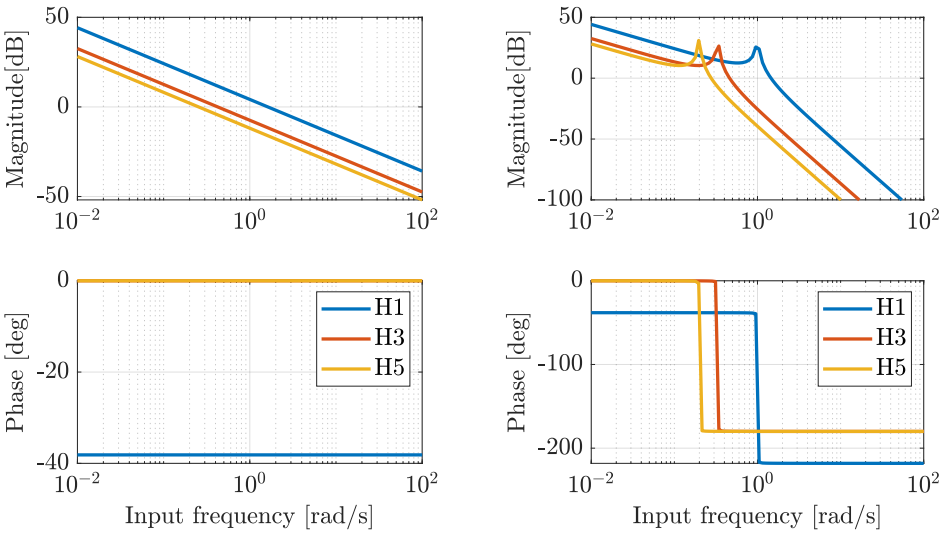

Figure 2.5: The importance of higher-order harmonics varies case by case.

components given by

$$\begin{aligned} \mathscr{C}(\omega) &= \mathscr{C}_{bl}(\omega) + \sum_{n=1}^{\infty} \mathscr{C}_{nln}(n\omega), \\ \mathscr{C}_{nln}(n\omega) &= 4M(\omega)R_{\delta}(n\omega)/(\pi n), \end{aligned} \tag{2.9}$$

where

$$\begin{aligned} M(\omega) &= \frac{\pi}{4} R_{\delta}^{-1}(\omega)\left[H_1(\omega) - C_{bl}(\omega)\right], \\ R_{\delta}(n\omega) &= C_R(jn\omega I - A_R)^{-1} jn\omega I. \end{aligned} \tag{2.10}$$

Furthermore, the higher-order sinusoidal describing functions for the closed-loop reset control system are developed in [23].

2.4. STABILITY ANALYSIS FOR RESET CONTROL SYSTEMS

In accordance with the H_β condition [15, 16, 23], the stability of the closed-loop RCS can be established as presented in Theorem 1.

Theorem 1. *A closed-loop reset control system is quadratically stable if and only if the H_β condition holds, that is, there exists a $\beta \in \mathbb{R}^r$ and a positive-definite $P_r \in \mathbb{R}^{r\times r}$ such that*

$$H_\beta(s) := \begin{bmatrix} P_r & 0_{r\times nr} & \beta C_p \end{bmatrix} (sI - A)^{-1} \begin{bmatrix} I_r \\ 0 \end{bmatrix} \tag{2.11}$$

is strictly positive real and closed-loop reset matrix $A_{\rho cl}$ satisfies the following condition:

$$A_{\rho cl}^T P_r A_{\rho cl} - P_r \leq 0 \tag{2.12}$$

2.5. APPLICATIONS OF RESET CONTROL

2.5.1. PI+CI

Reset controller systems have superior performance in both the time and frequency domains. However, in scenarios where the plant exhibits a steady-state error, the system's output demonstrates an undershoot behavior. This occurs because the reset action triggers when the output reaches the reference value. To address this, a combined PI+CI controller [6] can be employed. The linear controller (PI) addresses the steady-state error, while the reset controller diminishes the overshoot.

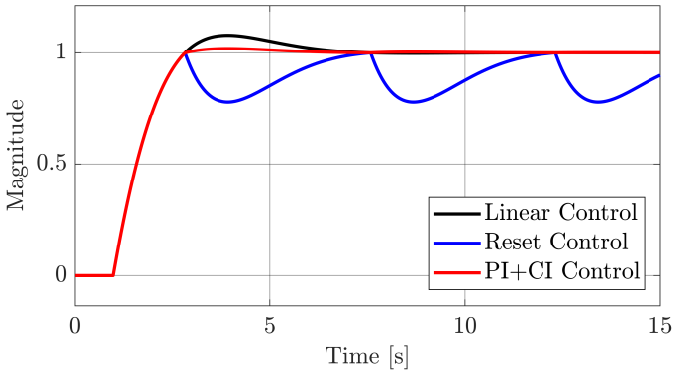

Figure 2.6: Step response comparison of the linear controller, reset controller, and PI+CI controller.

Figure 2.6 illustrates the step responses of three distinct controllers. It is evident that the PI+CI controller diminishes both the maximum overshoot and undershoot.

2.5.2. CgLp

Another application worth mentioning is the constant in gain lead in phase element (CgLp) [9]. This element offers a broadband phase lead without affecting the magnitude.

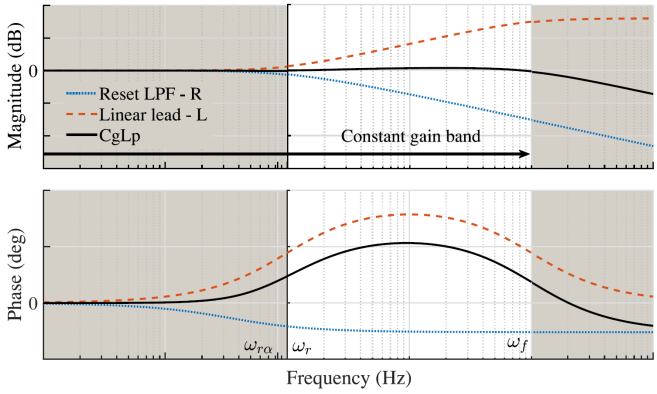

Figure 2.7: Frequency domain response of a generic CgLp element. [9]

Fig. 2.7 demonstrates that a CgLp comprises a lead-lag compensator and a reset controller. In terms of magnitude, the reset controller and lead-lag compensator possess equal slopes with opposite signs, effectively canceling out each other's effects and preserving the magnitude component. As the reset controller exhibits a lower phase lag than the linear controller, the combination of these two components yields a significant phase lead.

2.5.3. FIXED-INSTANT RESET CONTROL

The conventional reset control system, known as the zero-crossing reset law, resets the controller's output to zero when the input of the reset controller equals zero. This subsection introduces an alternative reset law, the fixed-instant reset law. Unlike the zero-crossing law, this law resets the controller's output at fixed time intervals, regardless of the input signal. The superior time-domain performance of FIRC has prompted extensive exploration, including its application in piezoelectric transducers [10] and unstable systems [12].

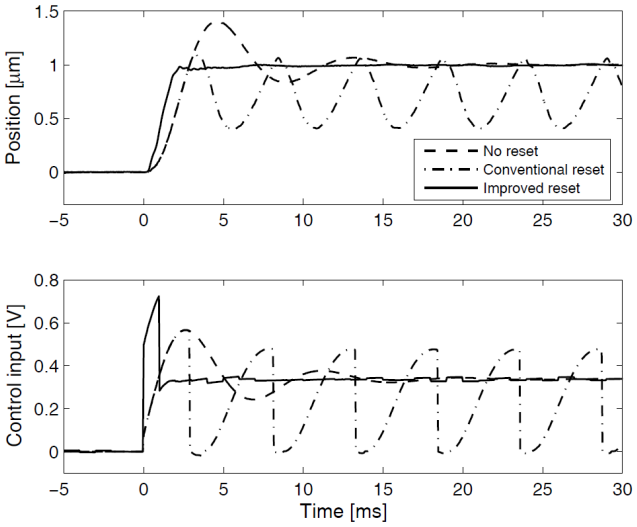

Figure 2.8: Step response comparison of PZT system with linear controller, conventional reset controller and FIRC controller. [10]

2.6. PROBLEM STATEMENT

FIRC systems demonstrate promising results in time-domain responses. However, there is currently a lack of frequency-domain analysis tools specifically tailored for FIRC systems. Given that the controller design process relies heavily on such frequency-domain analysis tools, this presents a significant challenge for FIRC systems.

Another downside of FIRC systems is that since the reset instants are predefined, certain frequencies cannot benefit from the reset action. Fig. 2.9 illustrates the output of a FIRC integrator with a reset instant of $\pi/2s$. It is evident that the input signal with a frequency of 1 rad/s benefits from FIRC, while the input signal with a frequency of 4 rad/s does not benefit from FIRC at all.

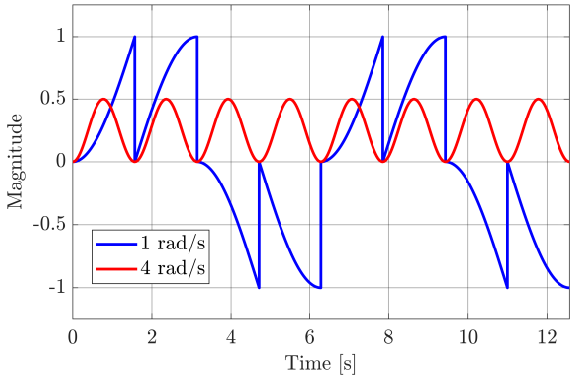

Figure 2.9: Demonstration of the downside of FIRC systems.

The upcoming chapter introduces the fixed-phase reset control law, which allows each input frequency to benefit from the reset action. Moreover, a frequency-domain analysis tool has been developed to facilitate the controller design process.

3

FIXED PHASE RESET CONTROL

Definition 1. *Fixed-phase reset control (FPRC) involves performing multiple resets within a single period, spacing each reset evenly in terms of phase, regardless of the input frequency. This approach ensures a uniform phase separation between consecutive reset instances. To quantify the number of resets, we introduce the variable k, denoting the reset count, with k taking values of 2h where h is an integer greater than or equal to 2 (i.e., $h = 2,3,4,...$).*

Our study is centered on the Single-Input-Single-Output (SISO) FPRC system, which is specifically designed for sinusoidal inputs. Given these assumptions and constraints, we can express the state space representation for FPRC systems as follows:

$$C = \begin{cases} \dot{x}_r(t) = A_R x_r(t) + B_R e(t), & t \notin U \\ x_r(t^+) = A_\rho x_r(t), & t \in U \\ u(t) = C_R x_r(t) + D_R e(t), \end{cases} \tag{3.1}$$

where U is a set of reset instants t_i.

$$U := \{t_i | t_i = \frac{2\pi i}{\omega k},\ i \in \mathbb{Z}^+\} \tag{3.2}$$

For simplicity, we denote $x_r(t_i)$ as m_i for the following content.

Definition 2. *The transfer function of the base-linear system (BLS) of the FPRC system is defined as*

$$R_L(\omega) = \frac{U_{bl}(\omega)}{E(\omega)} = C_R(j\omega I - A_R)^{-1} B_R + D_R, \tag{3.3}$$

where $U_{bl}(\omega)$ and $E(\omega)$ are the Fourier transform of the output and input signals of the reset controller.

3.1. FIX-PHASE RESET CONTROL ELEMENTS

In this paper, we apply three reset control structures applying our new Fix-phase (FP) resetting mechanisms. The new reset control elements are titled "Fix-phase Clegg Integrator (FP-CI)", "Fix-phase Clegg FORE (FP-FORE)", and "Fix-phase Second-order Single-State Reset Element (FP-SOSRE)" as illustrated below. The arrows in equations (3.5), (3.7), and (3.8) function as visual indicators, symbolizing the FR resetting actions.

3.1.1. FP-CI

The state-space matrices of FP-CI are

$$A_R = 0,\ B_R = 1,\ C_R = 1,\ D_R = 0, A_\rho = \gamma. \tag{3.4}$$

The transfer function symbol of FP-CI is given by

$$\frac{1}{s}. \tag{3.5}$$

3.1.2. FP-FORE

The state-space matrices of FP-FORE are

$$A_R = -\omega_{r\alpha},\ B_R = \omega_{r\alpha},\ C_R = 1,\ D_R = 0, A_\rho = \gamma. \tag{3.6}$$

The transfer function symbol of FP-FORE is given by

$$\frac{\omega_{\gamma\alpha}}{s+\omega_{\gamma\alpha}}. \tag{3.7}$$

3.1.3. FP-SECOND-ORDER SINGLE-STATE RESET ELEMENT (SOSRE)

Second-order single-state reset element, as demonstrated in equation (3.8) and depicted in Figure 3.1. The term "SOSRE" denotes a second-order reset element that resets the first state, namely x_2. "SOSRE" denotes a second-order reset element that resets the first state, x_2. The transfer function symbol of FP-SOSRE is given by

$$\frac{\omega_{\gamma\alpha}^2}{s^2+2\omega_{\gamma\alpha}s+\omega_{\gamma\alpha}^2}. \tag{3.8}$$

The state-space matrices of SOSRE are

$$\begin{aligned} A_R &= \begin{bmatrix} 0 & 1 \\ -\omega_{\gamma\alpha}^2 & -2\beta\omega_{\gamma\alpha} \end{bmatrix},\ B_R = \begin{bmatrix} 0 \\ \omega_{\gamma\alpha}^2 \end{bmatrix}, \\ C_R &= \begin{bmatrix} 1 & 0 \end{bmatrix},\ D_R = 0,\ A_\rho = \begin{bmatrix} \gamma & 0 \\ 0 & 1 \end{bmatrix}, \end{aligned} \tag{3.9}$$

where $\beta = 1$ in this case.

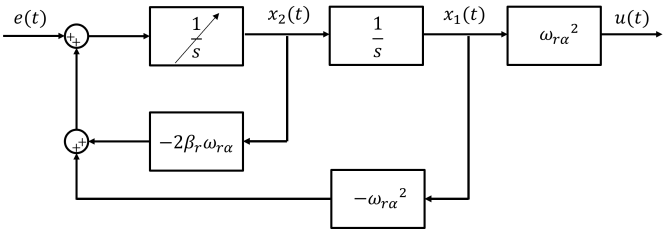

Figure 3.1: Block diagram of FP-SOSRE.

3.2. OPEN-LOOP HOSIDF FOR FPRC SYSTEMS

Lemma 1. *(Stair step wave model for FP-CI) The output signal $u(t)$ of a FP-CI system in (3.1) with $[A_R, B_R, C_R, D_R] = [0,1,1,0]$, $A_\rho = 0$, and $k = 4$, under the sinusoidal reference input $e(t) = \sin(\omega t)$ can be represented by its base-linear output ($u_{bl}(t)$) and a stair step wave ($q_{rc}(t)$). The stair step wave can be decomposed into two pulse waves while one has a 90° phase lead. Note that the phase shift of a pulse wave is defined relative to the $q_{rc}(t)$ of CI.*

Proof. The stair-step wave shown in Fig. 3.2c can be decomposed into two distinct pulse waves, as shown in Fig. 3.2d. Notably, the pulse wave depicted by the red line in Fig. 3.2d features a phase lead of 90°. □

Theorem 2. *As shown in Fig. 3.3, by applying the "Virtual Harmonics Generator", the periodical sinusoidal input $e(t) = |E|\sin(\omega t + \angle E)$ for the FPRC system is separated into harmonics $e_n(t)$ given by*

$$e_n(t) = |E|\sin(n\omega t + n\angle E), n \in \mathbb{Z}^+. \tag{3.10}$$

The HOSIDF for FPRC systems in (3.1) to describe the transfer function from the input $e(t)$ to the output $u(t)$ is given by

$$\widetilde{H}_n = \begin{cases} R_L(\omega) + \widetilde{\Phi}_1(\omega), & \text{for } n = 1 \\ \widetilde{\Phi}_n(n\omega), & \text{for odd } n \geq 2 \\ 0, & \text{for even } n \geq 2 \end{cases} \tag{3.11}$$

where

$$\begin{aligned} \widetilde{\Phi}_n(n\omega) &= \frac{4}{n\pi} R_\delta(n\omega)\widetilde{\Theta}_n(n\omega), \\ \widetilde{\Theta}_n(n\omega) &= \frac{1}{2}\sum_{l=0}^{\frac{k}{2}-1} m_{\frac{k}{2}-l}\exp(jn\frac{2\pi}{k}l), \\ R_\delta(n\omega) &= C_R(jn\omega I - A_R)^{-1} jn\omega I. \end{aligned} \tag{3.12}$$

m_i is given as follows for FPRC with different numbers (r) of states.

$$m_i = \begin{cases} m_{i-1}e^{A_R t_i} + [B_R e^{A_R t} * \sin(\omega t)]|_{t_i}, & \text{for } r = 1, \\ \mathscr{L}^{-1}\left\{\frac{E(s)+m_{i-1}(s+2\beta_r\omega_{r\alpha})}{s^2+2\beta_r\omega_{r\alpha}+\omega_{r\alpha}^2}\right\}|_{t_i}, & \text{for } r = 2. \end{cases} \tag{3.13}$$

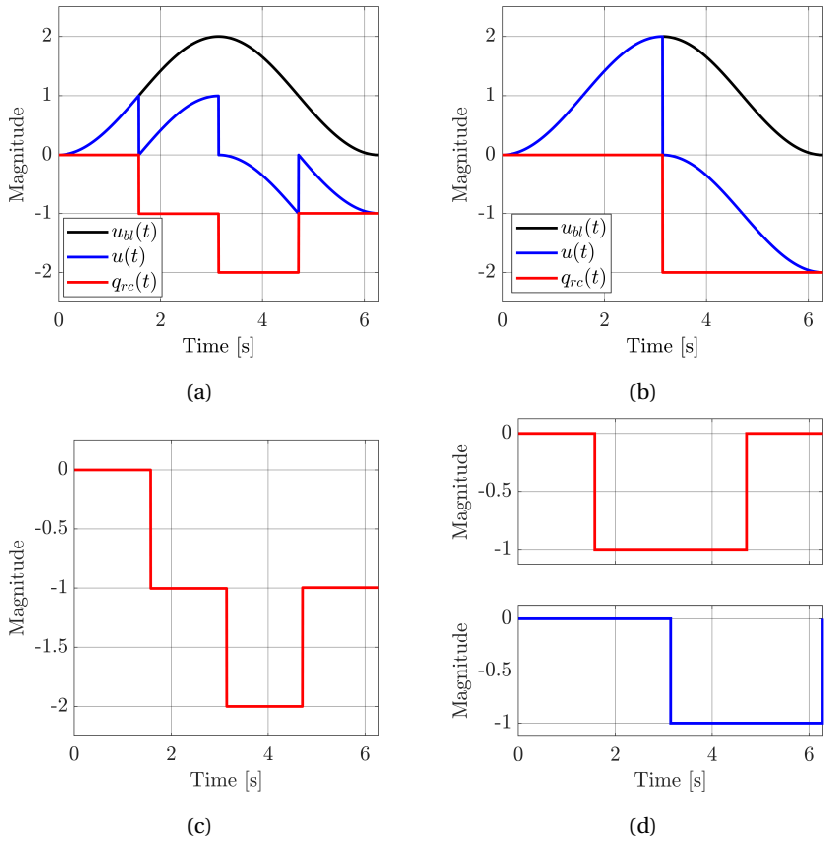

Figure 3.2: Time response comparison between a CI and a FP-CI with $k = 4$: (a) $u(t)$ of FP-CI and its components $u_{bl}(t)$ and $q_{rc}(t)$, (b) $u(t)$ of CI and its components $u_{bl}(t)$ and $q_{rc}(t)$, (c) $q_{rc}(t)$ of FP-CI, (d) Components of $q_{rc}(t)$ of FP-CI.

Proof. When calculating the amplitude m_i at reset instant t_i for FP-FORE, it is crucial to account for initial conditions. Each reset segment (from t_i to t_{i+1}) can be viewed as the linear output of the FORE with varying initial conditions and starting times. The calculation of m_i is provided below.

From (3.1), during $(t_i,\ t_{i+1})$, we have

$$\dot{x}_r(t) = A_R x_r(t) + B_R e(t). \tag{3.14}$$

The Laplace transform of (3.14) is given by

$$\begin{aligned} sX_r(s) - x_r(0) &= A_R X_r(s) + B_R E(s) \\ X_r(s) &= (s - A_R)^{-1}(x_r(0) + B_R E(s)). \end{aligned} \tag{3.15}$$

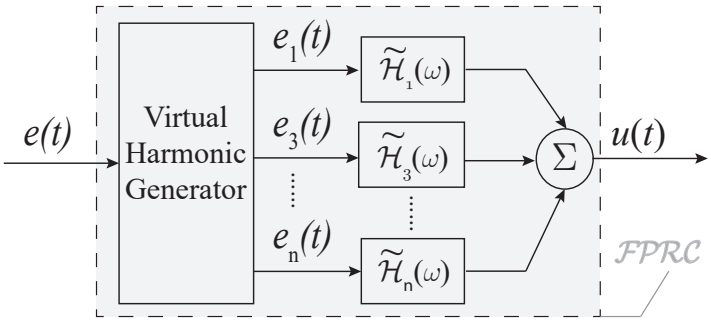

Figure 3.3: The HOSIDF for FPRC systems.

By conducting the inverse Laplace transform of (3.15), we have

$$x_r(t) = x_r(0)e^{A_R t} + [B_R e^{A_R t} * \sin(\omega t)](t). \tag{3.16}$$

Since the initial condition for m_i is m_{i-1}, the state value $x_r(t)$ at reset instant t_i denoted as m_i can be derived as follows:

$$m_i = m_{i-1}e^{A_R t_i} + [B_R e^{A_R t} * \sin(\omega t)]|_{t_i}, \tag{3.17}$$

as shown in (3.13). Note that the FP-CI is identical to the FP-FORE when $\omega_c = 0$, thus, equation (3.13) is also fit for the calculation for FP-CI.

The amplitude of the second state ($r = 2$) is calculated for FP-SOSRE. From (3.1), the state space representation of FP-SOSRE can be written as follows:

$$\begin{cases} \dot{x}_1 = x_2 \\ \dot{x}_2 = -2\beta_r\omega_{\gamma\alpha}x_2 - \omega_{\gamma\alpha}^2 x_1 + e(t) \end{cases} \tag{3.18}$$

Applying Laplace transform to both sides of the second equation of (3.18):

$$s^2 X_r(s) - s x_r(0) - \dot{x}_r(0) = A_R X_r(s) + B_R E(s) \tag{3.19}$$

Since $\dot{x}_r(0)$ is reset to zero,

$$X_r(s) = \frac{E(s) + x_r(0)(s + 2\beta_r\omega_{\gamma\alpha})}{s^2 + 2\beta_r\omega_{\gamma\alpha} + \omega_{\gamma\alpha}^2} \tag{3.20}$$

By conducting the inverse Laplace transform of (3.20), we get:

$$x_r(t) = \mathscr{L}^{-1}\left\{\frac{E(s) + x_r(0)(s + 2\beta_r\omega_{\gamma\alpha})}{s^2 + 2\beta_r\omega_{\gamma\alpha} + \omega_{\gamma\alpha}^2}\right\} \tag{3.21}$$

As stated above, the initial condition for m_i is m_{i-1}, and the state value $x_r(t)$ at reset instant t_i denoted as m_i can be derived as follows:

$$m_i = \mathscr{L}^{-1}\left\{\frac{E(s) + m_{i-1}(s + 2\beta_r\omega_{\gamma\alpha})}{s^2 + 2\beta_r\omega_{\gamma\alpha} + \omega_{\gamma\alpha}^2}\right\}|_{t_i} \tag{3.22}$$

Note that the choice of m_i for FP-SOSRE is discussed in Proposition 4 and Proposition 5.

From [23], $Q_{rc}(\omega)$ is written as follows:

$$Q_{rc}(\omega) = MQ_0(\omega) \tag{3.23}$$

where M is the amplitude of the pulse wave and $Q_0(\omega)$ is a unit pulse wave. In the case of FPRC, $Q_{rc}(\omega)$ comprises multiple $Q_0(\omega)$ components, with each having its unique amplitude and phase shift, as illustrated in Lemma 1.

Thus, we define a new parameter $\widetilde{\Theta}_n(n\omega)$ to denote the summation of the magnitude and phase shift of $Q_0(\omega)$. From Lemma 1, it can be seen that the $q_{rc}(t)$ of a FP-CI with $k = 4$ is composed of two pulse waves. Thus, a $q_{rc}(t)$ with k resets is composed of $k/2$ pulse waves.

The Fourier transform of a function $f(t)$ shifted in time can be written as follows:

$$\mathscr{F}\{f(t+a)u(t+a)\} = \exp(aj\omega)F(j\omega) \tag{3.24}$$

For FPRC, the time shift a can be written as follows:

$$a = \frac{2\pi}{\omega k}l \tag{3.25}$$

where $2\pi/(\omega k)$ represents the time interval between reset instants, and $l \in \mathbb{N}$ indicates the number of reset intervals a pulse wave should shift.

As previously explained, a $q_{rc}(t)$ with k resets consists of $k/2$ pulse waves. The $\frac{k}{2}^{th}$ pulse wave exhibits a zero phase shift, while the 1^{st} pulse wave features a phase shift of $\frac{k-2}{k}\pi$ radians.

It can be seen that from Fig. 3.2b, $q_{rc}(t)$ has an amplitude of -2. Thus, a scaling factor of $\frac{1}{2}$ is applied to $Q_0(\omega)$ to normalize it to unit amplitude.

Finally, $Q_{rc}(\omega)$ for FPRC can be written as follows:

$$\begin{aligned} Q_{rc}(\omega) &= \widetilde{\Theta}_n(n\omega)Q_0(\omega) \\ &= \frac{1}{2}\sum_{l=0}^{\frac{k}{2}-1} m_{\frac{k}{2}-l}\exp(jn\frac{2\pi}{k}l)Q_0(\omega) \end{aligned} \tag{3.26}$$

Since

$$Q_0(\omega) = \frac{4}{\pi}\sum_{n=1}^{\infty}\frac{E(n\omega)}{n} \tag{3.27}$$

$Q_{rc}(\omega)$ can be written as follows:

$$Q_{rc}(\omega) = \sum_{n=1}^{\infty}\frac{2}{n\pi}\sum_{l=0}^{\frac{k}{2}-1} m_{\frac{k}{2}-l}\exp(jn\frac{2\pi}{k}l)E(n\omega). \tag{3.28}$$

The reset output $u(t)$ is broken down into two distinct components: a linear segment denoted as $u_{bl}(t)$ and a filtered pulse component designated as $q_{ol}(t)$, given by

$$u(t) = u_{bl}(t) + q_{ol}(t). \tag{3.29}$$

Based on [23], $q_{ol}(t)$ and $q_{rc}(t)$ are given by

$$Q_{ol}(\omega) = R_\delta(n\omega)Q_{rc}(\omega). \tag{3.30}$$

where $R_\delta(n\omega)$ is given in (3.12).

By combining (3.3), (3.29), and (3.30), the output of the FPRC in the Fourier domain is given by

$$U(\omega) = R_L(\omega)E(\omega) + R_\delta(n\omega)Q_{rc}(\omega). \tag{3.31}$$

By defining $\widetilde{\Phi}_n(n\omega)$ and $\widetilde{\Theta}_n(n\omega)$ in (3.12), and combining with (3.28), the n-th transfer function of FPRC is defined as

$$\widetilde{H}_n(\omega) = \frac{U(n\omega)}{E(n\omega)} = \frac{2}{n\pi}R_\delta(n\omega)\sum_{l=0}^{\frac{k}{2}-1} m_{\frac{k}{2}-1}\exp(jn\frac{2\pi}{k}l)$$

as shown in (3.11).

□

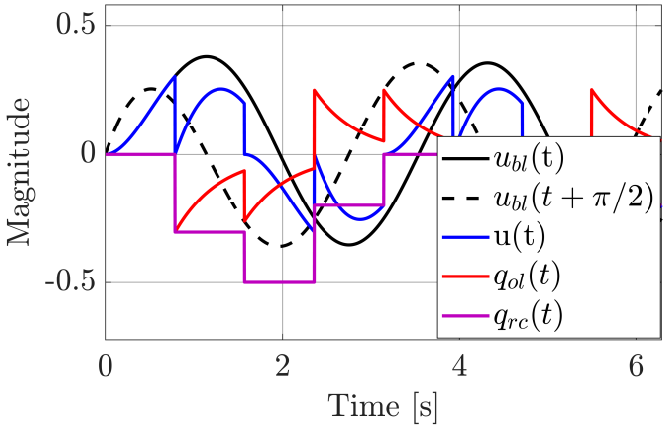

Figure 3.4: Time response of a PF-FORE with $k = 4$.

Proposition 4. *In contrast to FORE, the output of FP-SOSRE displays transient behavior 3.5. We assume the second cycle is at stead-state for simplicity, but one can select other cycles for greater precision if necessary.*

Proof. The BLS of the FP-SOSRE ($k = 4$) of Fig. 3.5 is written as follow:

$$\frac{U_{bl}(s)}{E(s)} = \frac{1}{s^2 + 2\beta s + 1} \tag{3.32}$$

In this case, $\beta = 1$. The relation between $x_2(t), x_{2,bl}(t)$ and $x_{2,nl}(t)$ is shown below.

$$x_2(t) = x_{2,bl}(t) + x_{2,nl}(t) \tag{3.33}$$

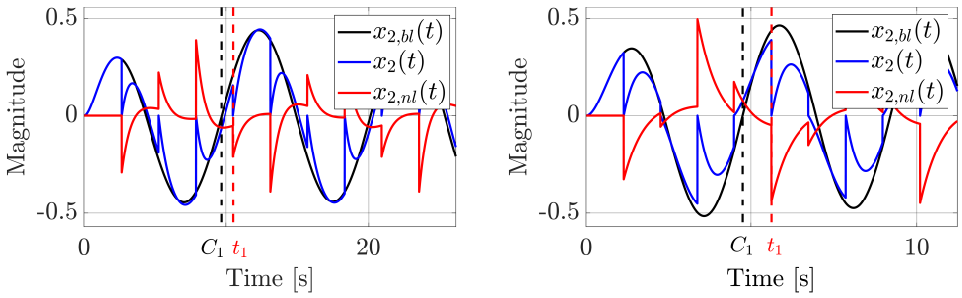

(a) (b)

Figure 3.5: Time response of a FP-SOSRE with $k = 4$: The red dash lines indicate the chosen t_1 reset instants. The end of the first cycle is marked by the black dash line. (a) Fourth reset instant selected as t_1, (b) Fifth reset instant selected as t_1.

It's evident that FP-SOSRE exhibits transient behavior. To verify if the chosen $x_2(t_1)$ is settled, a simulation was performed. Note that for FP-SOSRE, $x_2(t_1) = m_1$. The duration of a "cycle" is defined as the duration in which the base linear output crosses zero twice.

The simulation in Fig. 3.6 serves two purposes: firstly, to determine if the second cycle is accurate enough to be chosen as the steady-state cycle, and secondly, to assess whether the coefficient β has an impact on this outcome.

To enhance readability, we normalize the results as follows: if the input frequency (ω_{in}) is less than 1 rad/s (the corner frequency of FP-SOSRE), we divide the results by the input frequency; for input frequencies greater than or equal to 1 rad/s, we multiply the results by the input frequency.

Fig. 3.6 shows m_1 at each cycle with different β and ω_{in}. The deviation of m_1 between the second and the eleventh cycle is shown in TABLE 3.1. It can be seen that the highest deviation is not even greater than 5%. Thus, the small deviations caused by assuming the second cycle is settled can be neglected. □

Proposition 5. *The selection of the first reset instant, denoted as t_1, should vary with input frequency ω_{in}.*

Proof. For the following proof, the period (T) of an input frequency ω_{in} is defined as follows:

$$T = \frac{2\pi}{\omega_{in}} \tag{3.34}$$

The duration of the first cycle is denoted as C_1. If $C_1 < T$, the first cycle is considered incomplete; if $C_1 > T$, the first cycle is considered complete.

The transfer function of $E(s)$ to $X_{2,bl}(s)$ for (3.32) can be written as follow:

$$\frac{X_{2,bl}(s)}{E(s)} = \frac{s}{s^2 + 2s + 1} \tag{3.35}$$

Deviation (%)			
ω_{in} \ β	1	0.1	0.01
0.01 rad/s	0	0	2.98e-5
0.1 rad/s	0	2.93e-3	8.58e-6
1 rad/s	2.17	3.49e-3	4.82e-7
10 rad/s	3.4e-1	4.1e-1	4.2e-1
100 rad/s	5.33e-5	5.45e-5	5.46e-5

Table 3.1: The deviation of m_1 between the second and the eleventh cycle.

By employing $e(t) = \sin(\omega_{in} t)$ as input signals, we categorize the results into three cases.
Case 1: $\omega_{in} < 1$

$$\angle\left(\frac{X_{2,bl}(s)}{E(s)}\right) \in (0°, 90°) \Longrightarrow \frac{3}{4}T < C_1 < T \tag{3.36}$$

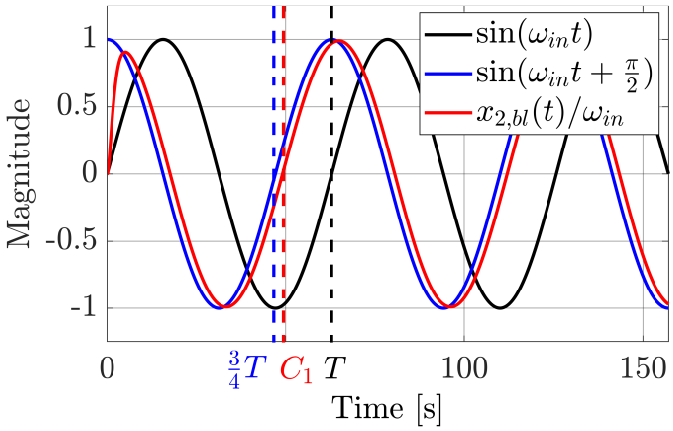

Figure 3.7: Comparison of C_1 and T when $\omega_{in} = 0.1$ rad/s.

Case 2: $\omega_{in} = 1$

$$\angle\left(\frac{X_{2,bl}(s)}{E(s)}\right) = 0° \Longrightarrow T = C_1 \tag{3.37}$$

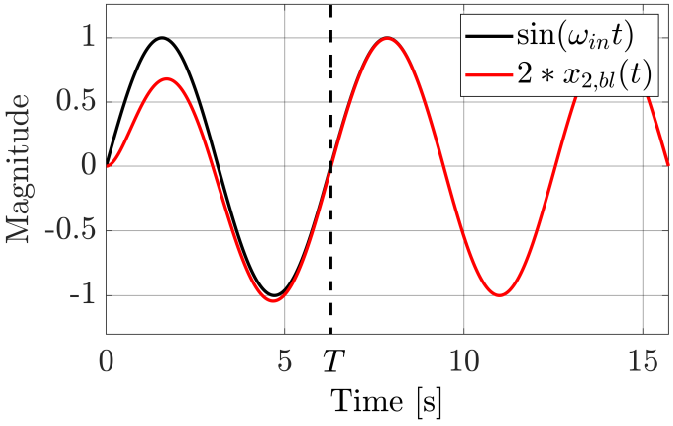

Figure 3.8: Comparison of C_1 and T when $\omega_{in} = 1$ rad/s.

Case 3: $\omega_{in} > 1$

$$\angle\left(\frac{X_{2,bl}(s)}{E(s)}\right) \in (-90°, 0°) \Longrightarrow T < C_1 < \frac{5}{4}T \tag{3.38}$$

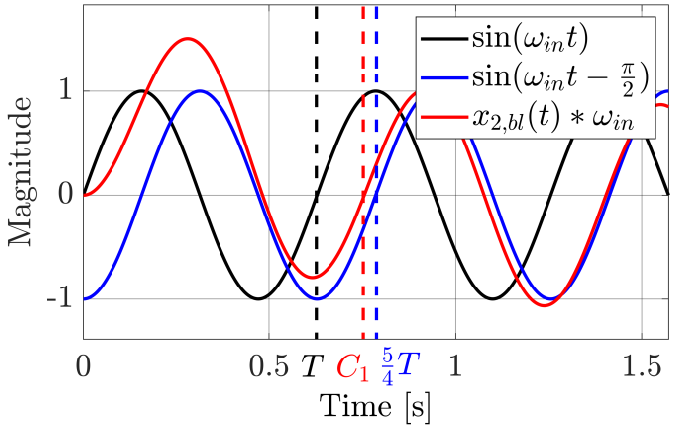

Figure 3.9: Comparison of C_1 and T when $\omega_{in} = 10$ rad/s.

In the case of FP-SOSRE with $k = 4$, the reset interval is 90°, equivalent to $T/4$. Therefore, for $\omega_{in} < \omega_c$, the duration of C_1 can only accommodate three reset points. The

fourth reset instant is only included when $C_1 \geq T$. In other words, for $k = 4$, the magnitude of the fifth reset instant is chosen as m_1 if the input frequency is equal to or greater than the corner frequency.

As shown in Fig. 3.5a, where $C_1 < T$, it can only contain three reset instants. In contrast, Fig. 3.5b shows that $C_1 > T$, allowing it to encompass four reset instants. This distinction is particularly relevant for the case of $k = 4$, and users should choose the initial reset instance based on the specific reset count in their application. □

3.3. CLOSED-LOOP HOSIDF FOR FPRC SYSTEMS

In [23], closed-loop sensitivity functions were established for reset control systems ((3.39),(3.40)). Since the FPRC model is based on the pulse model, this framework can serve as our closed-loop model as well. Nevertheless, as indicated in Fig. 3.3, the output signal of an FPRC system exhibits multiple frequencies due to the virtual harmonic generator.

$$S_n(\omega) = \begin{cases} \frac{1}{1+\mathscr{L}_O(\omega)}, & \text{for } n = 1 \\ -\frac{\Gamma\mathscr{L}_{NL}(n\omega)}{1+\mathscr{L}_O(n\omega)} \frac{1}{1+\mathscr{L}(n\omega)}, & \text{for odd } n \geq 2 \\ 0, & \text{for even } n \geq 2 \end{cases} \tag{3.39}$$

$$T_n(\omega) = \begin{cases} \frac{\mathscr{L}_O(\omega)}{1+\mathscr{L}_O(\omega)}, & \text{for } n = 1 \\ \frac{\Gamma\mathscr{L}_{NL}(n\omega)}{1+\mathscr{L}_O(n\omega)} \frac{1}{1+\mathscr{L}(n\omega)}, & \text{for odd } n \geq 2 \\ 0, & \text{for even } n \geq 2 \end{cases} \tag{3.40}$$

with

$$\begin{aligned} \mathscr{L}_O(n\omega) &= \mathscr{L}(n\omega) + \Gamma\mathscr{L}_{NL}(n\omega) \\ \Gamma &= 1/(1 - \frac{\sum_{n=3}^{\infty}\zeta(n\omega)\eta(n\omega)}{\eta(\omega)}) \\ \zeta(n\omega) &= \frac{-|\mathscr{L}_{NL}(n\omega|}{1+\mathscr{L}(n\omega)} \\ \eta(n\omega) &= (A_\rho - I)|R_L(n\omega)|\sin(l\pi + \angle(R_L(n\omega))) \end{aligned}$$

where $l \in \mathbb{N}$.

Given that FPRC is specifically designed for Single-Input-Single-Output (SISO) inputs, this situation poses a challenge. To ensure the valid application of closed-loop FPRC, we need to make the assumption that the amplitudes of higher-order harmonics are relatively small, thereby simplifying the feedback signal to essentially one frequency.

Given that our primary focus does not lie in the closed-loop aspect, we will not delve deeply into this part, reserving it for future work.

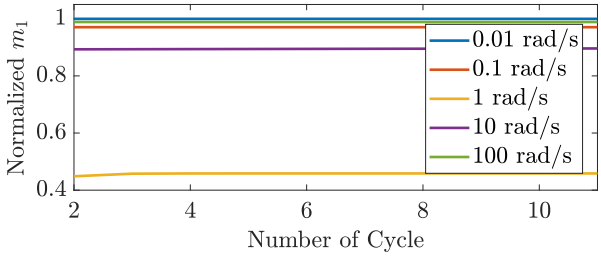

(a)

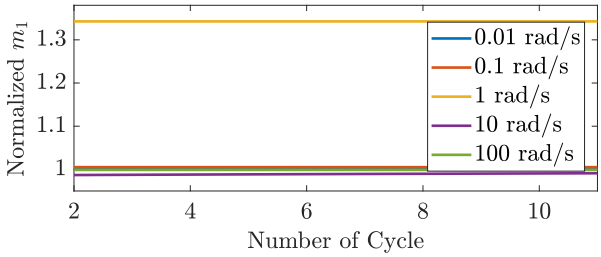

(b)

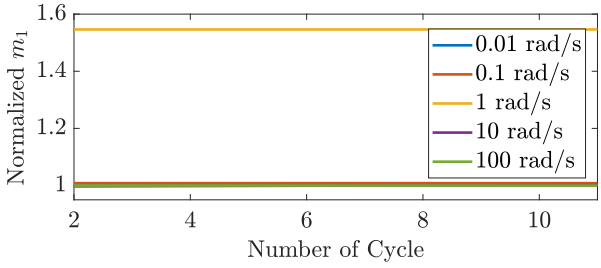

(c)

Figure 3.6: Normalized m_1 at each cycle with different input frequencies and values of β. (a) $\beta = 1$, (b) $\beta = 0.1$, (c) $\beta = 0.01$

4

THE ACCURACY OF THE HOSIDF FOR FPRC

To validate the accuracy of the HOSIDF for the FPRC system, several simulations were conducted to assess the disparities between the output of the DF and HOSIDF compared to the simulated outputs. The BLS for FP-CI, FP-FORE, and FP-SOSRE, are $1/s$, $1/(s+1)$, and $1/(s^2+2s+1)$, respectively. Each of the HOSIDF outputs contains seven harmonics.

4.1. FREQUENCY RESPONSE-BASED PREDICTION

Fig. 4.1a and Fig. 4.1b illustrate the frequency responses of the FP-FORE and FP-SOSRE models used in the simulation. Notably, higher-order harmonics in both FP-FORE and FP-SOSRE become negligible when the input frequency is below the corner frequency. When the input frequency exceeds the corner frequency, FP-FORE exhibits behavior similar to FP-CI, maintaining a consistent magnitude gap of 7.8 dB between the first and third-order harmonics. FP-SOSRE, on the other hand, shows a larger magnitude gap of 17.8 dB. Therefore, we anticipate observing minimal nonlinear characteristics at lower input frequencies and clear reset edges at higher input frequencies.

4.2. TIME DOMAIN RESULTS

The time responses shown in Fig. 4.2, Fig. Fig. 4.3, and Fig. 4.4 validate that HOSIDF outputs closely align with the simulated outputs, confirming the accuracy of our HOSIDF. In contrast, the DF output fails to capture the reset edge. Notably, Fig. 4.3 and Fig. 4.4 are in line with our expectations.

Note that Fig. 4.2 and Fig. 4.3 show the outputs of $u(t)$, while Fig. 4.4 shows the outputs of $x_2(t)$.

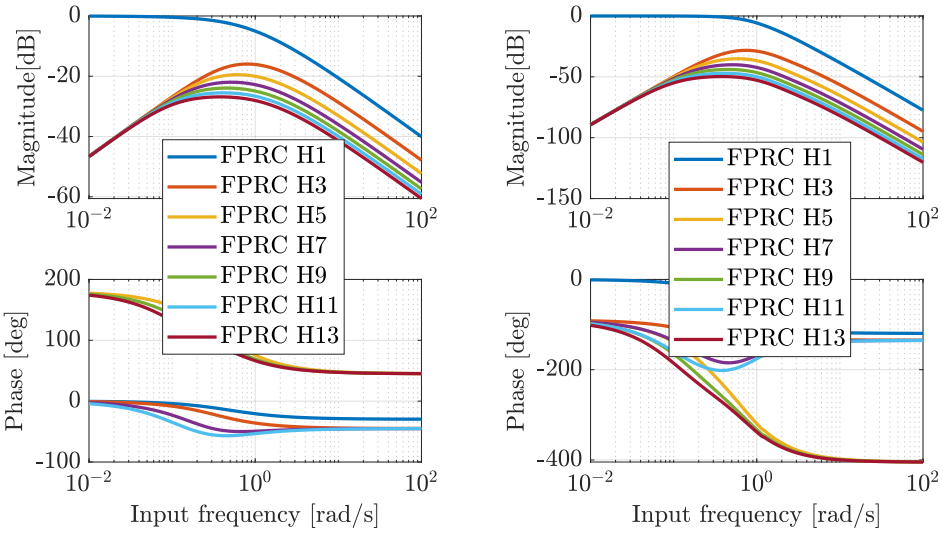

Figure 4.1: (a) Frequency response of FP-FORE with $k = 4$. (b) Frequency response of FP-SOSRE with $k = 4$ and $\beta = 1$.

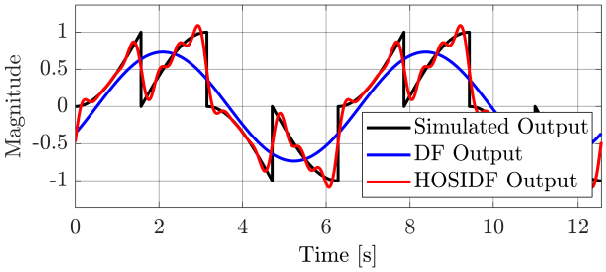

Figure 4.2: Comparison of the time responses for the DF output of FP-CI, HOSIDF output of FP-CI, and the simulated output of FP-CI ($\omega_{in} = 1$ rad/s).

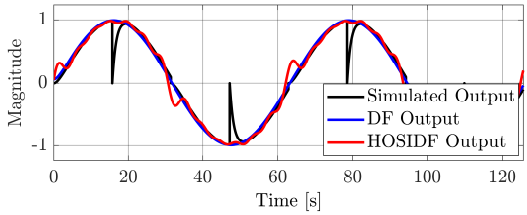

(a)

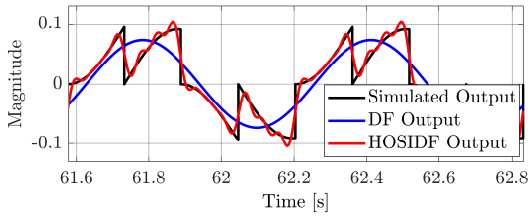

(b)

Figure 4.3: Comparison of the time responses for the DF output of FP-FORE, HOSIDF output of FP-FORE, and the simulated output of FP-FORE. (a) $\omega_{in} = 0.1$ rad/s, (b) $\omega_{in} = 10$ rad/s.

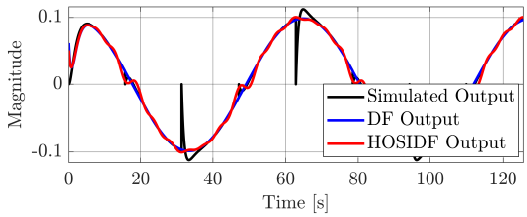

(a)

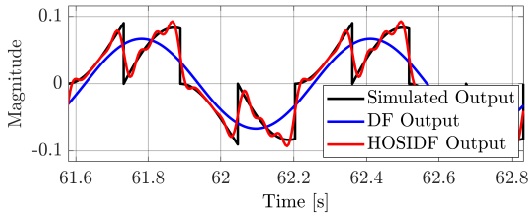

(b)

Figure 4.4: Comparison of the time responses for the DF output of FP-SOSRE, HOSIDF output of FP-SOSRE, and the simulated output of FP-SOSRE. (a) $\omega_{in} = 0.1$ rad/s, (b) $\omega_{in} = 10$ rad/s.

5

ILLUSTRATIVE EXAMPLES

This chapter provides a numerical simulation to demonstrate the effectiveness of the FPRC reset law. In this simulation, a second-order MSD system with a time delay is utilized as the plant, while the controller employs a CgLp element [9], a PID controller, and a low-pass filter.

5.1. PRECISION MOTION STAGE

The "Spyder" precision positioning stage, illustrated in Fig. 5.2, serves as the validation platform for this study. We approximate the transfer function of the "Spyder" system described in (5.1) as a simplified single eigenmode mass-spring-damper model using Matlab's identification tool.

$$P(s) = \frac{9836e^{-0.0001s}}{s^2 + 8.737s + 7376}. \tag{5.1}$$

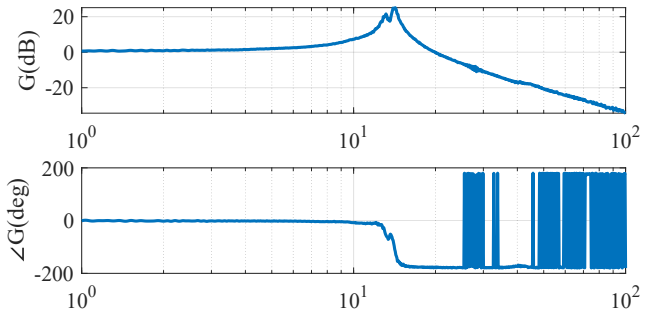

Figure 5.1: FRF of the "Spyder" system.

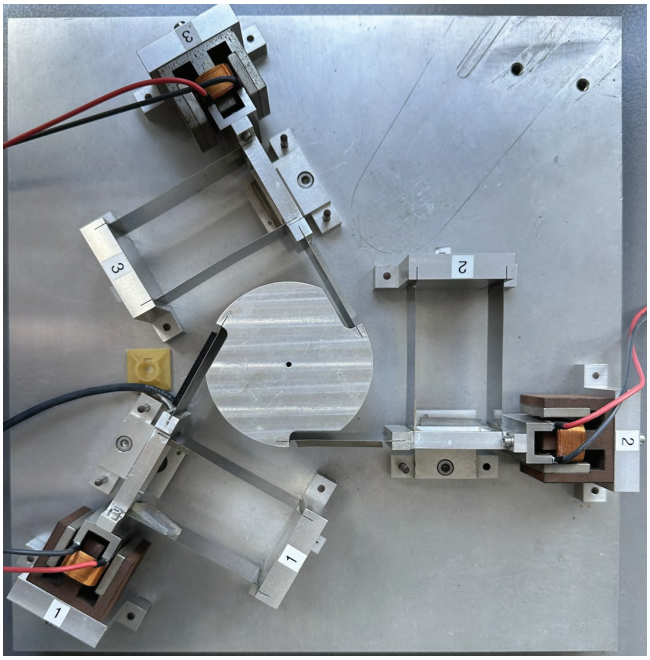

Figure 5.2: The planar precision positioning system, named as “Spyder”utilizes three voice coil actuators denoted as A_1, A_2, and A_3. Each actuator is mechanically connected to a corresponding mass represented by M_1, M_2, and M_3. These masses are linked exclusively to the base M_C, through dual leaf flexures. Position feedback from the masses is obtained through linear encoders referred to as “Enc”.

5.2. CONTROL SYSTEM DESIGN

The designed open-loop control system shown in Fig. 5.3 is described by the following base-linear transfer function:

$$L(s) = \text{CgLp} * C(s) * \text{LPF} * P(s), \tag{5.2}$$

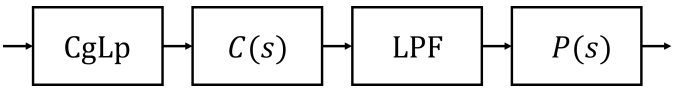

Figure 5.3: Open-loop block diagram of the simulation system.

where

$$\begin{aligned} \text{CgLp} &= \frac{1}{\frac{s}{\omega_{\gamma\alpha}}+1}\frac{\frac{s}{\omega_\gamma}+1}{\frac{s}{100\omega_\gamma}+1}, \\ C(s) &= K_p(1+\frac{\omega_i}{s})\frac{\frac{s}{\omega_d}+1}{\frac{s}{\omega_t}+1}, \\ \text{LPF} &= \frac{1}{\frac{s}{\omega_f}+1}. \end{aligned} \tag{5.3}$$

The parameters used in the system are designed to achieve a bandwidth of 150 rad/s and phase margin of 50°, given by

$$\begin{aligned} &\omega_\gamma = \omega_c,\ \omega_i = \frac{\omega_c}{10},\ \omega_d = \frac{\omega_c}{d},\ \omega_t = d\omega_c,\ \omega_f = 10\omega_c, \\ &K_p = 70.95355,\ d = 3.477562. \end{aligned} \tag{5.4}$$

Figure 5.4 compares the frequency responses of the linear integrator, CI, and FP-CI with $k = 4$. Notably, CI exhibits a gain of 1.62, while FPRI has a gain of 0.733. This discrepancy in gain results in a shift in the corner frequency for FORE and SOSRE, necessitating the introduction of a compensation factor denoted as α [27] to compensate the open-loop gain, given by

$$\omega_{\gamma\alpha} = \frac{\omega_\gamma}{\alpha}. \tag{5.5}$$

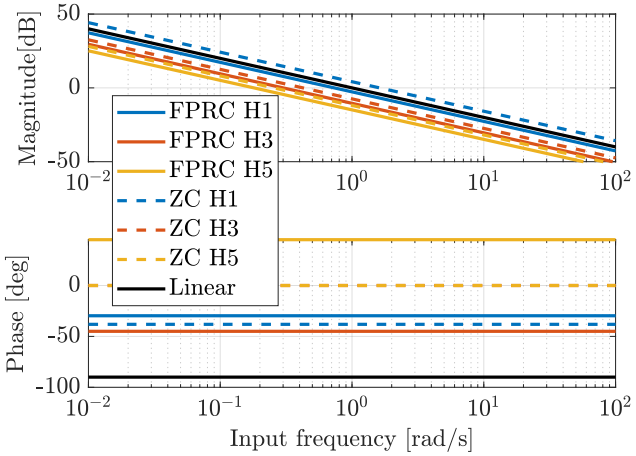

Figure 5.4: Frequency response comparison among the linear integrator, CI, and FPRI with $k = 4$.

5.3. FREQUENCY DOMAIN ANALYSIS FOR FPRC

Figure 5.5 shows the open-loop frequency response comparison of the FPRC system, the RC system with zero-crossing law, and the linear system. They are designed to achieve the same gain and bandwidth as the first-order harmonic in open-loop. In this paper, we chose two cases ($k = 4$ and $k = 20$) to illustrate the effectiveness of k.

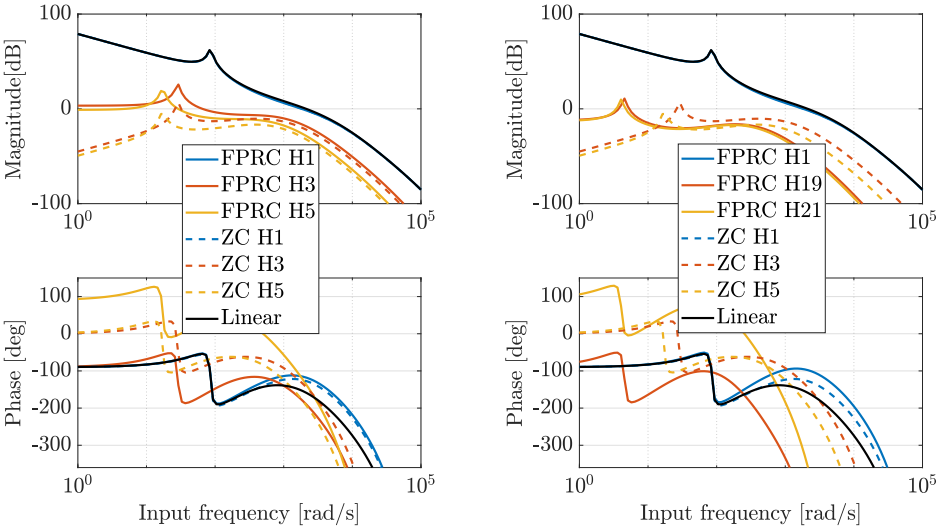

Figure 5.5: Comparison of the open-loop frequency responses of the base linear system, the zero-crossing system, and the FPRC system for two cases: (a) $k = 4$, (b) $k = 20$.

Remark 1. *The larger the k, the smaller the phase lag of an FPRC element.*

It is evident that when $k = 4$, the FPRC system demonstrates a larger phase margin compared to the ZC system, amounting to an approximate 9° reduction in phase lag. In the case of $k = 20$ however, a considerable distinction emerges between them, with a significant 30° reduction in phase lag.

Remark 2. *The magnitude of certain higher-order harmonics becomes negligible as the value of k increases.*

Fig. 5.5 illustrates that the third and fifth harmonics possess significant magnitudes when $k = 4$. However, in the case of $k = 20$, the nineteenth and twenty-first harmonics are the two harmonics with magnitudes substantial enough to be notable, surpassed only by the first-order harmonic. Thus, these two harmonics are the practical third and fifth harmonics.

Remark 3. *The magnitudes of higher-order harmonics decrease as k increases.*

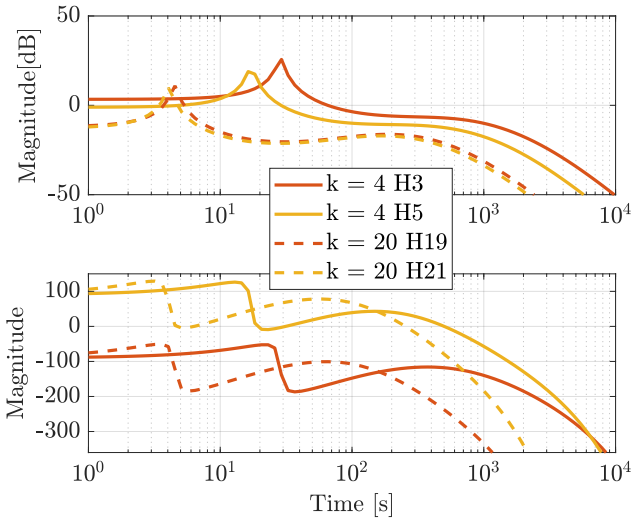

Figure 5.6: Higher-order harmonics comparison of case $k = 4$ and case $k = 20$.

It can be seen that from Fig. 5.6, for the case of $k = 4$, the magnitudes of the third and fifth harmonics remain consistently greater than the higher-order harmonics in the case of $k = 20$, starting from 10 rad/s.

Considering these observations, it becomes apparent that a larger value of k tends to yield better results. Nevertheless, it's essential to recognize that the first-order harmonic of an FPRI with $k = 20$ already exhibits a minimal 6° phase lag. This suggests that further increasing the value of k is unlikely to significantly reduce the phase lag.

5.4. TIME DOMAIN ANALYSIS

Fig. 5.7 illustrates the disparity between the cases of $k = 4$ and $k = 20$. In the $k = 20$ scenario, the output closely resembles a pure sine wave, while in the case of $k = 4$, the output exhibits edges, a consequence of the involvement of higher-order harmonics.

Remark 4. *The magnitude of the first-order harmonics of an FPRC system experiences a slight reduction when the input signal is close to the corner frequency of the reset element.*

From Fig. 5.7, it can be seen that the output from the FPRC system, whether in the case of $k = 4$ or $k = 20$, exhibits a lower amplitude compared to the linear output.

Remark 5. *The FPRC system can deliver satisfactory performance when the input signal includes a sinusoidal signal along with a small level of magnitude.*

A triangle wave can be written as follows:

$$x(t) = \frac{-8}{\pi^2} \sum_{n=1}^{\infty} \frac{(-1)^n}{(2n-1)^2} \sin(2\pi(2n-1)t) \tag{5.6}$$

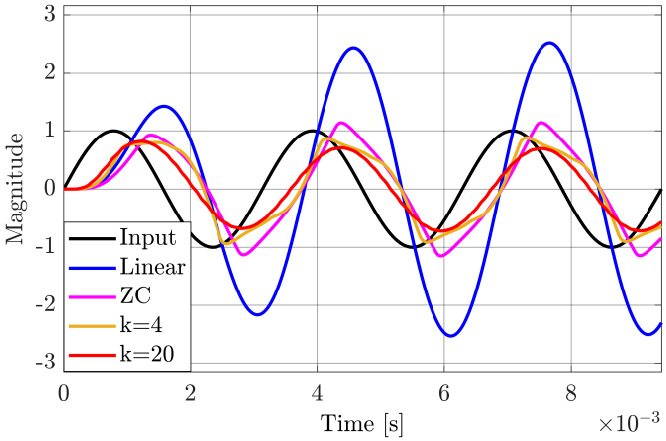

Figure 5.7: Comparison of the time responses of the closed-loop linear system, the closed-loop ZC system, and the closed-loop FPRC system under a 2000 rad/s sine wave input.

Similar to a square wave, a triangle wave consists solely of odd-numbered harmonics. However, its higher-order harmonics follow an inverse proportionality to the square of the harmonic number, unlike the square wave, where the inverse proportionality is with the harmonic number itself. This suggests that a triangle wave can be viewed as comprising a sine wave with noise.

The result of the FPRC system under triangular reference input is shown in Fig. 5.8. The result demonstrates that FPRC with $k = 20$ exhibits superior tracking ability and the smallest phase lag.

5.5. ASSESSMENT OF TRACKING ABILITY

To further assess the tracking performance under varying input frequencies, Fig. 5.9 and Fig. 5.10 depict the root-mean-squared error and the infinity-normed error for sine wave inputs.

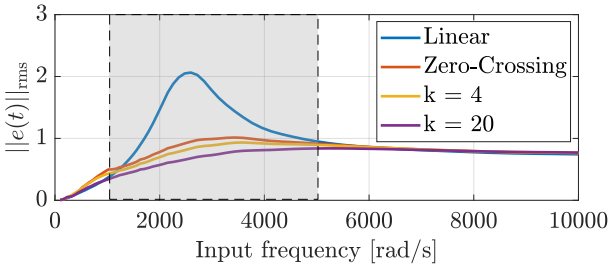

Figure 5.9: Root-mean-squared error analysis with sine wave input.

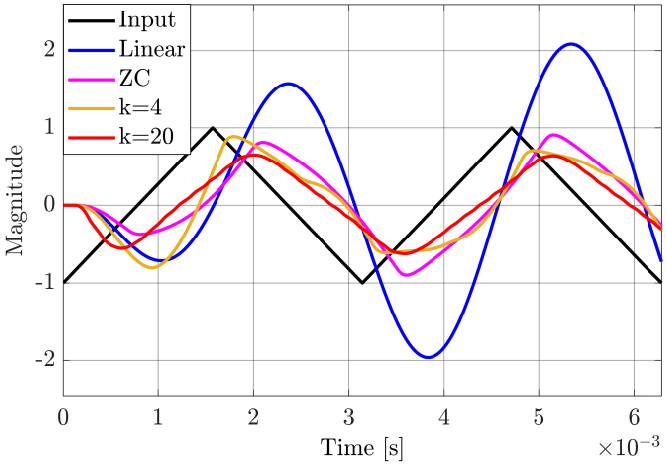

Figure 5.8: Comparison of the time responses of the closed-loop linear system, the closed-loop ZC system, and the closed-loop FPRC system under a 2000 rad/s triangle wave input.

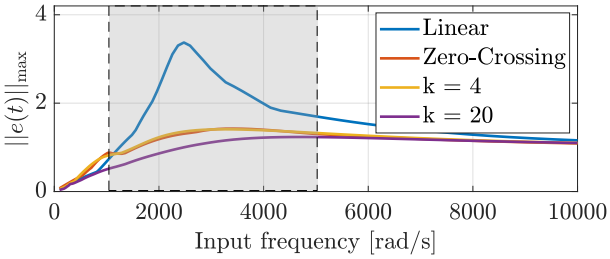

Figure 5.10: Infinity-normed error analysis with sine wave input.

Both the root-mean-squared error and the infinity-normed error indicate that the performance of the $k = 20$ case surpasses that of the others within the frequency range of 1000 rad/s to approximately 5000 rad/s, which effectively encompasses the plant's operational frequencies. Conversely, within the frequency range of 0 rad/s to 1000 rad/s, both the ZC system and the FPRC system exhibit slightly inferior performance compared to the linear system. This is attributed to the influence of higher-order harmonics.

Both the reset element of ZC and FPRC systems share a common corner frequency of 150 Hz, approximately equivalent to 942.5 rad/s, which is very close to 1000 rad/s. Therefore, it can be inferred that both the ZC and FPRC systems exhibit superior tracking performance when the input signal frequency surpasses their respective corner frequencies.

It's worth noting that the results for triangle wave inputs align with the trends observed in sine wave inputs. This similarity suggests that a triangle wave can serve as a suitable input signal for FPRC systems.

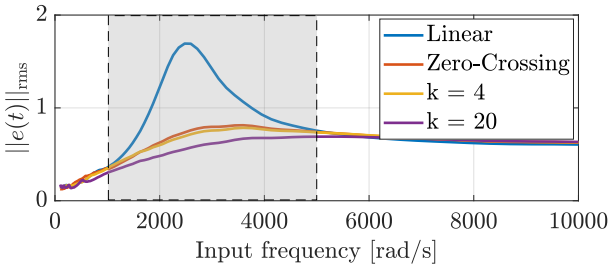

Figure 5.11: Root-mean-squared error analysis with triangle wave input.

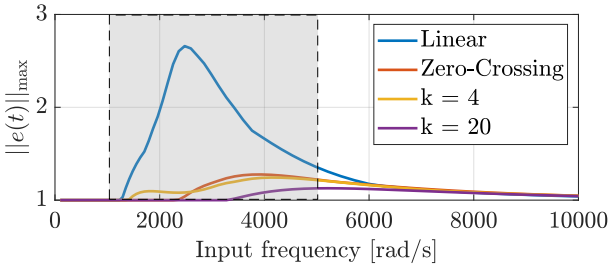

Figure 5.12: Infinity-normed error analysis with triangle wave input.

5.6. ASSESSMENT OF CONVERGING ABILITY

In addition to tracking ability, we are also interested in improving settling time. Since the FPRC system exhibits superior performance in the frequency range of 1000 rad/s to 5000 rad/s (as shown in Fig. 5.9, Fig. 5.10, Fig. 5.11, Fig. 5.12)), we assess whether the FPRC also demonstrates superior settling time performance in this frequency range.

Since the input signal is a periodic signal, a normalized settling time is defined to assess their converging ability. It is defined as the time it takes for u(t) to pass through 0 for the nth time, divided by the duration of one cycle of the input signal.

$$\text{normalized } t_s = \frac{t_{0,n}}{T_\omega} \tag{5.7}$$

where

$$t_{0,n} = \text{time of nth zero-crossing of u(t)} \tag{5.8}$$

$$T_\omega = \text{time for one cycle of the input signal at frequency } \omega. \tag{5.9}$$

Fig. 5.13 illustrates a comparison of settling times for both sine wave and triangle wave inputs. In this case, $t_{0,6}$ is used to calculate their normalized t_s, which represents the time of the 6th zero-crossing of u(t). If greater accuracy is required, one can choose a larger value of n. The trends in both figures consistently show that the case with $k = 20$ exhibits the shortest settling time in the frequency range of 2000 rad/s to 5000 rad/s.

However, when the input frequency falls below 2000 rad/s, regardless of whether the input signal is a sine wave or a triangle wave, the linear system performs slightly better than the FPRC system with $k = 20$.

In conclusion, FPRC systems indeed demonstrate improvements in both the frequency and time domains. Nevertheless, it is important to identify the appropriate range of input frequencies to leverage the advantages of this new reset law fully.

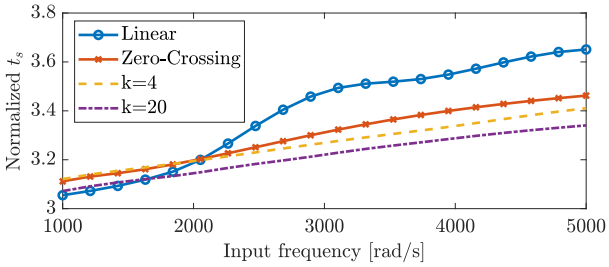

(a)

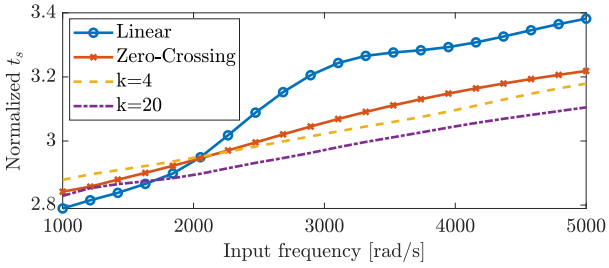

(b)

Figure 5.13: Normalized settling times for two different input waveforms: (a) sine wave input, (b) triangle wave input.

6

CONCLUSION

6.1. SUMMARY

This paper introduces a novel reset law of fixed-phase reset control (FPRC), which operates by resetting at specific times determined by the input frequency and reset count. FPRC is specifically designed for Single-Input-Single-Output systems with sinusoidal inputs. To facilitate the controller design process, we have developed a frequency domain analysis tool. Furthermore, numerical simulations have been conducted to assess the impact of the FPRC reset law. The evaluation criteria encompass tracking ability, measured through root-mean-squared error and infinity-normed error, and converging ability, quantified by a newly defined normalized settling time.

6.2. DISCUSSION

Our findings clearly demonstrate the superior performance of FPRC systems in both tracking and converging capabilities. Notably, our experiments with triangle wave inputs have yielded results consistent with those obtained with sine wave inputs. This suggests the adaptability of FPRC to handle sine wave inputs with noise or periodic signals comprising a dominant sine wave alongside lower amplitude harmonics.

6.3. LIMITATIONS AND FUTURE WORK

The limitation of FPRC lies in its constrained input compatibility. To function effectively, the input signal must predominantly consist of a specific frequency, with minimal amplitudes at other frequencies. Deviations from this criterion necessitate the use of distinct controllers, as the input frequency significantly impacts reset timing. Future research endeavors should prioritize the development of frequency separators to enhance the versatility of FPRC across a broader array of applications.

BIBLIOGRAPHY

[1] ASML,"Mechanics & Mechatronics", https://www.asml.com/en/technology/lithography-principles/mechanics-and-mechatronics

[2] K. Aström and R. Murray, Feedback Systems: An Introduction for Scientists and Engineers. Princeton University Press, 2010.

[3] J. C. Clegg, A nonlinear integrator for servomechanisms, Transactions of the American Institute of Electrical Engineers, Part II: Applications and Industry 77 (1958) 41–42.

[4] Isaac Horowitz and Patrick Rosenbaum. Non-linear design for cost of feedback reduction in systems with large parameter uncertainty. International Journal of Control, 21(6):977–1001, 1975.

[5] KR Krishnan and IM Horowitz. Synthesis of a non-linear feedback system with significant plant-ignorance for prescribed system tolerances. International Journal of Control, 19(4):689–706, 1974.

[6] Alfonso Banos and Angel Vidal. Definition and tuning of a pi+ ci reset ~ controller. In 2007 european control conference (ECC), pages 4792– 4798. IEEE, 2007.

[7] Leroy Hazeleger, Marcel Heertjes, and Henk Nijmeijer. Second-order reset elements for stage control design. In 2016 American Control Conference (ACC), pages 2643–2648. IEEE, 2016.

[8] Saikumar, Niranjan, and Hassan HosseinNia. "Generalized fractional order reset element (GFrORE)." 9th European Nonlinear Dynamics Conference (ENOC). 2017.

[9] N. Saikumar, R. K. Sinha, S. H. HosseinNia, “constant in gain lead in phase” element–application in precision motion control, IEEE/ASME Transactions on Mechatronics 24 (2019) 1176–1185.

[10] M. F. Y. W. J. Zheng, Y. Guo and L. Xie., Improved Reset Control Design for a PZT Positioning Stage. 2007 IEEE International Conference on Control Applications, 2007.

[11] A. Baños, F. Perez and J. Cervera, "Network-Based Reset Control Systems With Time-Varying Delays," in IEEE Transactions on Industrial Informatics, vol. 10, no. 1, pp. 514-522, Feb. 2014

[12] D. Paesa, J. Carrasco, O. Lucia and C. Sagues, "On the design of reset systems with unstable base: A fixed reset-time approach," IECON 2011 - 37th Annual Conference of the IEEE Industrial Electronics Society, Melbourne, VIC, Australia, 2011, pp. 646-651

[13] D. Paesa, A. Baños, C. Sagues, Optimal reset adaptive observer design, Systems & Control Letters, Volume 60, Issue 10, 2011, Pages 877-883, ISSN 0167-6911.

[14] Y. Guo, Y. Wang, L. Xie, H. Li and W. Gui, "Optimal reset law design of reset control systems with application to HDD systems," Proceedings of the 48h IEEE Conference on Decision and Control (CDC) held jointly with 2009 28th Chinese Control Conference, Shanghai, China, 2009, pp. 5287-5292, doi: 10.1109/CDC.2009.5399857.

[15] Yuqian Guo, Youyi Wang, Lihua Xie, Jinchuan Zheng, Stability analysis and design of reset systems: Theory and an application, Automatica, Volume 45, Issue 2, 2009, Pages 492-497, ISSN 0005-1098, https://doi.org/10.1016/j.automatica.2008.08.016.

[16] O. Beker, C. Hollot, Y. Chait, H. Han, Fundamental properties of reset control systems, Automatica 40 (2004) 905–915.

[17] H. Hu, Y. Zheng, Y. Chait and C. V. Hollot, "On the zero-input stability of control systems with Clegg integrators," Proceedings of the 1997 American Control Conference (Cat. No.97CH36041), Albuquerque, NM, USA, 1997, pp. 408-410 vol.1, doi: 10.1109/ACC.1997.611829.

[18] Ali Ahmadi Dastjerdi, Alessandro Astolfi, and S Hassan HosseinNia. A frequency-domain stability method for reset systems. In 2020 59th IEEE Conference on Decision and Control (CDC), pages 5785–5791. IEEE, 2020.

[19] Y. Guo, Y. Wang, and L. Xie, “Frequency-domain properties of reset systems with application in hard-disk-drive systems,” IEEE Transactions on Control Systems Technology, vol. 17, pp. 1446–1453, Nov 2009.

[20] Kars Heinen. Frequency analysis of reset systems containing a clegg integrator: An introduction to higher order sinusoidal input describing functions. 2018.

[21] P. Nuij, M. Steinbuch, O. Bosgra, Measuring the higher order sinusoidal input describing functions of a non-linear plant operating in feedback, Control Engineering Practice 16 (2008) 101–113.

[22] P. Nuij, O. Bosgra, M. Steinbuch, Higher-order sinusoidal input describing functions for the analysis of non-linear systems with harmonic responses, Mechanical Systems and Signal Processing 20 (2006) 1883–1904.

[23] Xinxin Zhang, Marcin B Kaczmarek, and S Hassan HosseinNia. Frequency-domain analysis for reset systems using pulse-based model. arXiv preprint arXiv:2206.00523, 2022.

[24] N. Karbasizadeh, A. A. Dastjerdi, N. Saikumar, D. Valério and S. H. Hossein Nia, "Benefiting from Linear Behaviour of a Nonlinear Reset-Based Element at Certain Frequencies," 2020 Australian and New Zealand Control Conference (ANZCC), Gold Coast, QLD, Australia, 2020, pp. 226-231, doi: 10.1109/ANZCC50923.2020.9318363.

[25] X. Zhang and S. H. HosseinNia, "Frequency-domain Analysis for Infinite Resets Systems*," 2023 IEEE International Conference on Mechatronics (ICM), Loughborough, United Kingdom, 2023, pp. 1-6, doi: 10.1109/ICM54990.2023.10101919.

[26] Niranjan Saikumar, Kars Heinen, S. Hassan HosseinNia, Loop-shaping for reset control systems: A higher-order sinusoidal-input describing functions approach, Control Engineering Practice, Volume 111, 2021, 104808, ISSN 0967-0661, https://doi.org/10.1016/j.conengprac.2021.104808.

[27] N. Karbasizadeh and S. Hassan HosseinNia, "Stacking Integrators Without Sacrificing the Overshoot in Reset Control Systems," 2022 American Control Conference (ACC), Atlanta, GA, USA, 2022, pp. 893-899, doi: 10.23919/ACC53348.2022.9867231..

[28] A. Gelb and W. E. V. Velde., Multiple-Input Describing Functions and Nonlinear System Design. McGraw-Hill, 1968.

[29] A. A. Dastjerdi, A. Astolfi, N. Saikumar, N. Karbasizadeh, D. Valerio, S. H. HosseinNia, Closed-loop frequency analysis of reset control systems, arXiv preprint arXiv:2001.10487 (2020).

[30] Y. Guo, L. Xie, Y. Wang, Analysis and Design of Reset Control Systems, 2015. doi:10.1049/PBCE094E.